SCIENCE CHINA
Information Sciences

• RESEARCH PAPER •

March 2024, Vol. 67, Iss. 3, 132402:1–132402:10
https://doi.org/10.1007/s11432-023-3810-9

Experimental demonstration of a photonic spiking neuron based on a DFB laser subject to side-mode optical pulse injection

Shuiying XIANG[1*], Shuang GAO[1], Yuechun SHI[2*], Yuna ZHANG[1], Ziwei SONG[1], Xingxing GUO[1], Yahui ZHANG[1], Yuxin MA[3] & Xiangfei CHEN[3]

[1]*State Key Laboratory of Integrated Service Networks, Xidian University, Xi'an* 710071*, China;*
[2]*Yongjiang Laboratory, Ningbo* 315202*, China;*
[3]*College of Engineering and Applied Sciences, Nanjing University, Nanjing* 210023*, China*

Received 28 February 2023/Revised 14 April 2023/Accepted 5 June 2023/Published online 19 February 2024

Abstract We proposed and experimentally demonstrated a simple and novel photonic spiking neuron based on a distributed feedback (DFB) laser subject to side-mode optical pulse injection (SMOPI). The DFB laser chip is designed and fabricated based on asymmetric equivalent π phase shift (π-EPS) with the reconstruction-equivalent-chirp (REC) technique. Under side-mode continuous-wave (CW) optical injection, excitability pulse was experimentally observed during the dominant mode switching process due to the injection-locked effect. Based on the transition between the excitability regime and the side-mode injection locking effect, the controllable and repeatable neuron-like spiking response can be realized when external stimulus pulses are electro-optically modulated on the CW optical carrier. The experimental results show that the spike threshold, temporal integration, and refractory period, which are important spike processing mechanisms in biological neurons, can all be achieved in the optically-injected DFB laser. The experimental findings are also verified numerically with a rate equation model that considers the SMOPI. To the best of our knowledge, this is the first experimental demonstration of a photonic spiking neuron based on a DFB laser subject to SMOPI, which holds promise for realizing large-scale photonic spiking neuron arrays for hardware photonic spiking neural network chips.

Keywords neuromorphic photonics, photonic spiking neuron, DFB laser, side-mode optical pulse injections

1 Introduction

With the rapid development of machine learning and artificial intelligence, huge amounts of data are generated and need to be processed in real-time. Traditional processors based on the von-Neumann architecture are hard to meet these requirements. Neuromorphic computing has become a promising paradigm for non von Neumann computing and has made significant progress [1–3]. Photonics neuromorphic computing shows obvious advantages of high-speed and energy efficiency [4–8], but is still in its infancy.

In general, linear optical computation has made great progress [9–15], but nonlinear optical computation is difficult and still remains a significant challenge [16, 17]. In recent years, there have been various successful demonstrations of photonic neural chips, but the focus is mainly limited to the implementation of weight matrix multiplication. Note that, in a photonic neural network, if the nonlinear computation is not implemented in the optical domain, the optical-electronic-optical (O/E/O) conversion and analog-to-digit/digit-to-analog (AD/DA) conversion are still required, resulting in additional system power consumption and latency. To address this issue, there are tremendous efforts towards nonlinear computation for photonic neural networks. So far, the photonic spiking neuron, which is a basic building block of a photonic spiking neural network (SNN), has been demonstrated with polarization switching vertical-cavity surface-emitting lasers (VCSELs) [18–25], VCSEL with saturable absorber [26–28],

* Corresponding author (email: jxxsy@126.com, yuechun-shi@ylab.ac.cn)

© Science China Press 2024

micropillar lasers [29, 30], integrated two-section distributed feedback (DFB) laser [31, 32], integrated Fabry-Perot laser with saturable absorber [33,34], silicon photonics micro-ring or microresonator [35–37], and phase-change material based integrated devices [38]. However, each above-mentioned solution shows its limitation (please see a review in [39] for more detail). It is still open to exploring a novel photonic spiking neuron that is suitable for large-scale integrated photonic SNN.

DFB laser is one of the most commonly used optical sources in optical communication systems [40]. A single-section DFB laser has been demonstrated to act as a graded-potential-signaling photonic neuron [41]. However, the conventional single-section DFB laser has not been applied to realize a photonic spiking neuron. The DFB laser technology is mature and easy to realize large-scale integration. Shi et al. [42] have successfully fabricated a multi-wavelength DFB laser array with up to 60 channels. Thus, the DFB laser is a very promising candidate for large-scale photonic spiking neuron arrays. The working principle, operating conditions, and physical mechanisms of photonic spiking neurons based on the DFB laser deserve further study.

In this article, we proposed and experimentally demonstrated a photonic spiking neuron based on a DFB laser subject to side-mode optical pulse injection (SMOPI). The mechanisms underlying the neuron-like spiking response are revealed, and the operating conditions leading to the neuron-like dynamics are identified experimentally. The rest of the paper is organized as follows. Section 2 describes the fabrication of the DFB laser chip and the experimental setup for testing the photonic spiking neuron based on the DFB laser with SMOPI. Section 3 presents the experimental results of the excitability dynamics and neuron-like spiking response. The excitable spiking threshold, temporal integration, and refractory period results are presented. The numerical model and results are shown in Section 4. Finally, the overall conclusion is summarized in Section 5.

2 Device fabrication and experimental setup

The schematic diagram of the fabricated DFB laser and the sample of the DFB laser chip are illustrated in Figures 1(a) and (b). The epitaxial wafer structure consists of an n-InP substrate, a buffer layer, an InGaAsP passive slab layer, two separate confinement heterostructure (SCH) layers, multiple quantum wells (MQWs) with compressive strain quantum wells (QWs) and tensile strain quantum barriers (QBs), an InGaAsP grating layer, and a p-InP cladding layer. The doping concentration is optimized to reduce plasma light loss. Anti-reflection (AR) and high-reflection (HR) coating are applied to improve light emission power. The grating is designed with sampled grating. We shift the half-period of the sampling structure to the location of 20% side of the HR facet. This sampled grating structure can equivalently introduce π phase shift (π-EPS) [43]. Here, the π-EPS is realized by the reconstruction-equivalent-chirp (REC) technique. Compared to the conventional electron beam lithography (EBL), the REC technique offers obvious advantages of low cost and precise wavelength control. Note, the threshold of the DFB laser fabricated with the REC technique may be slightly increased due to the relatively small grating coupling coefficient, but can be partly compensated by designing a thick grating layer. The DFB laser chip is further packaged, and is then tested for emulating a photonic spiking neuron.

The experimental setup for testing the DFB laser subject to SMOPI is shown in Figure 1(c). A tunable laser (TL) generated continuous-wave (CW) optical carrier. The packaged DFB laser is biased with a laser diode controller (LDC: ILX Lightwave LDC3724B) that provides a low-noise bias current and precise temperature control. The CW light was injected into an intensity modulator, and an arbitrary wave generator (AWG, Tektronix AWG70001A) produced the designed external electronic stimulus. The modulation speed of the Mach-Zehnder modulator (MZM) is 10 GHz. Two polarization controllers (PCs) were employed before and after the intensity modulator to match the polarization state. Then the modulated optical signal was injected into the DFB laser without isolation through a three-port optical circulator. The optical spectrum was measured by the optical spectrum analyzer (OSA, Advantest Q8384). Two photodetectors (PDs, Agilent/HP 11982A), with operating bandwidth being 15 GHz, were employed to realize the optical-electronic conversion, and a real-time oscilloscope (OSC, Keysight DSOZ592A) was utilized to measure the time series.

The measured power-current (PI) curve is shown in Figure 1(d). The threshold current is about 44 mA. The optical spectrum of a free-running DFB laser is presented in Figure 1(e). The side mode suppression ratio is about 52 dB. To obtain the neuron-like spiking response, the wavelength of the optical injected signal needs to be properly adjusted. Here, the target side mode is different from the free-running

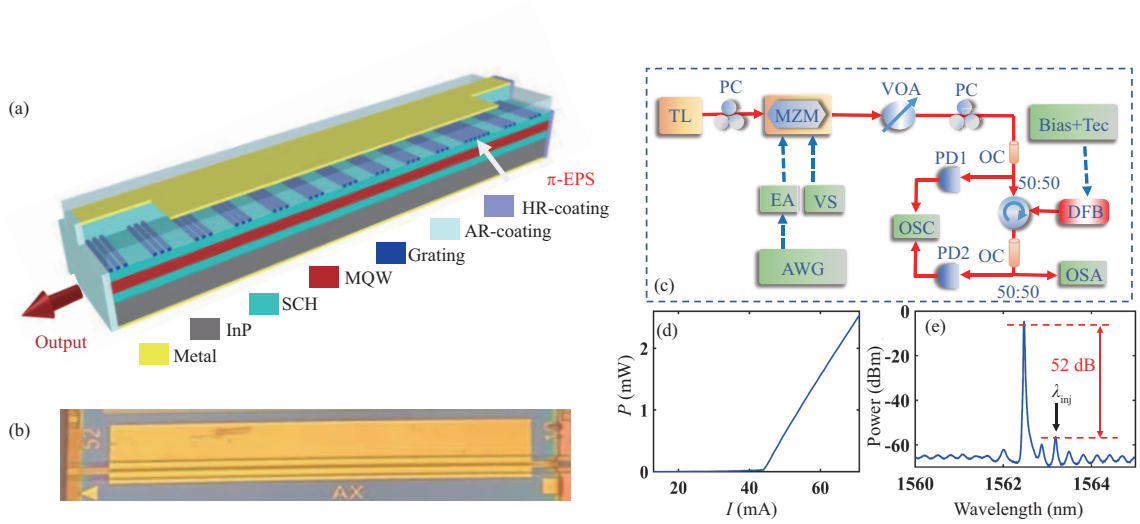

Figure 1 (Color online) Fabrication and experimental setup for the DFB-based photonic spiking neuron. (a) Schematic diagram of the fabricated DFB laser based on asymmetric π-EPS; (b) sample of fabricated DFB laser chip; (c) experimental setup for a photonic spiking neuron based on DFB laser with SMOPI; (d) measured PI curve; (e) measured optical spectrum of the free-running DFB laser. VOA: variable optical attenuator; EA: electronic amplifier; VS: voltage source; OC: optical coupler.

dominant mode. The strongest side mode (denoted by the arrow) is chosen as the target mode as shown in Figure 1(e), and the wavelength of TL is set to be slightly higher than the target mode wavelength.

3 Results and discussion

To begin with, we explored the nonlinear dynamics of the DFB laser subject to side mode CW optical injection. The excitability and injection locking effects are mainly considered. Here, the AWG shown in Figure 1(c) is turned off. As presented in Figure 2, with the side mode CW optical injection, single-pulse or multiple-pulse excitability can be achieved. The excited output consists of bursts with different numbers of spikes, which agrees well with the theoretical prediction [44]. Note, such single- or multi-pulse excitability originates from the homoclinic bifurcation point [45,46].

Near the random excitability regime, the periodic excitable spike output can also be observed when the injected power or bias current is varied. A representative periodic spike sequence is shown in Figure 3(a). By fixing the injected light power, we find that the spike frequency is slightly varied with the bias current. The spike frequency as a function of bias current is presented in Figure 3(b). We can find that, the spike frequency is not fixed, multiple frequency values can be observed in experiments, which may be associated with the intrinsic noise.

Next, the injected power of the CW carrier is set close to the homoclinic bifurcation point. Then, we turned on the AWG, and the defined external stimulus signal was modulated on the optical carrier. To show the spike threshold property of the DFB-based photonic spiking neuron, we define a pulse sequence with gradually-increasing stimulus strength as shown in Figure 4(a). Note, similar to [21], the stimulus is encoded as power drops, and the stimulus strength is defined as $K_p = (V_{\rm CW} - V_s)/V_{\rm CW}$. Here, as denoted in Figure 4(a), $V_{\rm CW}$ represents the amplitude of the CW state, while V_s denotes the amplitude of the power drops. Here, the calculated K_p for the five input stimulus pulses is 0.1969, 0.2799, 0.4096, 0.4536, and 0.4985, respectively. As can be seen in Figures 4(b1)–(b7), for a given fixed bias current, the spike response can be well-controlled by the injected power. We can tune the injected power to make the DFB laser respond with a controllable spike number. More specifically, the number of triggered spikes is decreased gradually with the increase of injected power. When $P_{\rm inj} = 360.5$ μW, the injected power is relatively small, both the CW injection and the power drops injection cannot reach the threshold of the injection-locked state, and the DFB laser operates in the periodic pulse state. Here, the self-pulsation frequency shown in Figure 4(b1) is 562 MHz. Then, for $P_{\rm inj} = 383.5$ μW, the CW state can force the DFB laser to operate in the injection-locked state, while all the power drop stimuli cannot reach the threshold of the injection-locked state. Thus, for each stimulus period, 5 spikes respond to the 5 stimulus power drops. When the $P_{\rm inj}$ is increased further, the response spike number in one stimulus period is 4, 3,

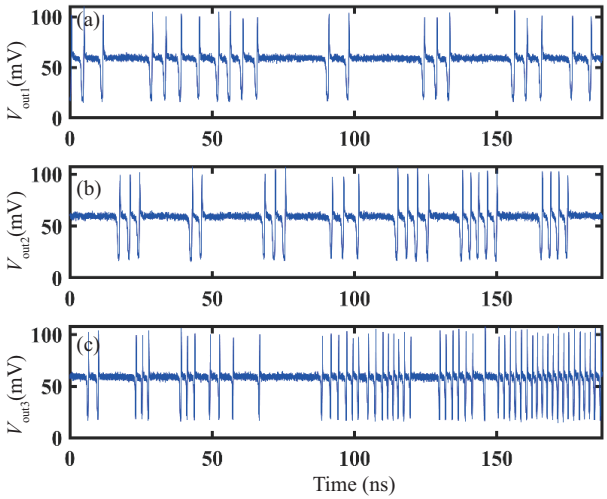

Figure 2 (Color online) Excited pulses in a DFB laser subject to side-mode CW optical injection.

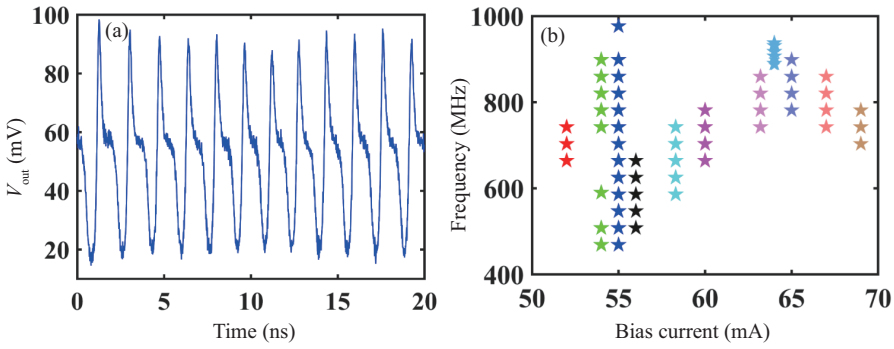

Figure 3 (Color online) (a) Time series of period spike output; (b) spike frequency as a function of the bias current.

2, and 1, respectively. That is, the excitable spiking threshold of the K_p is increased for a higher injected power. Note, that if the stimulus pulse triggers a response spike, the spike amplitude is independent of the stimulus pulse intensity. As shown in Figure 4(b7), for $P_{\text{inj}} = 591.8$ μW, no large-amplitude spike is generated as it is completely injection-locked by the external optical stimulus. Here, the dynamics of the DFB laser change from the excitability regime into the injection-locked states with the increase of injected power.

In addition, we also present the corresponding optical spectra during the transition process. As shown in Figures 4(c1)–(c3), due to the SMOPI, the injected wavelength becomes the dominant mode of the DFB laser, while the original peak wavelength is broadened to some extent, and the power is lower than the injected wavelength. In addition, the suppression ratio, defined as the difference between two peaks, increases with the increasing stimulus strength. Thus, a controllable spike threshold behavior similar to that observed in a biological neuron can be achieved in the DFB laser with SMOPI. Interestingly, this neuron-like spiking behavior based on the transition between the excitability dynamics and injection-locked state is also similar to the findings observed in the polarization switching VCSEL [18, 21]. In the present scheme, the dominant longitudinal mode is hopped to the injected side mode to obtain the neuron-like dynamics. In the VCSEL, the dominant polarization mode is switched between two polarization modes to realize a photonic spiking neuron. These two laser-based spiking neurons have their own advantages and disadvantages. For the VCSEL-based photonic spiking neuron, the power consumption is low, and it can be large-scale integrated, but its output power is relatively low. For the DFB laser-based photonic spiking neuron, it can be integrated planarly with the mainstream silicon photonics-based weight network. Besides, the output power of the DFB laser is much higher than that of the VCSEL, which is highly desirable for integrated photonic SNN chips as loss is a critical factor.

Subsequently, the temporal integration behavior is demonstrated experimentally. As shown in Figure 5(a), we defined three input stimuli. The stimulus strength is relatively low, and thus each single

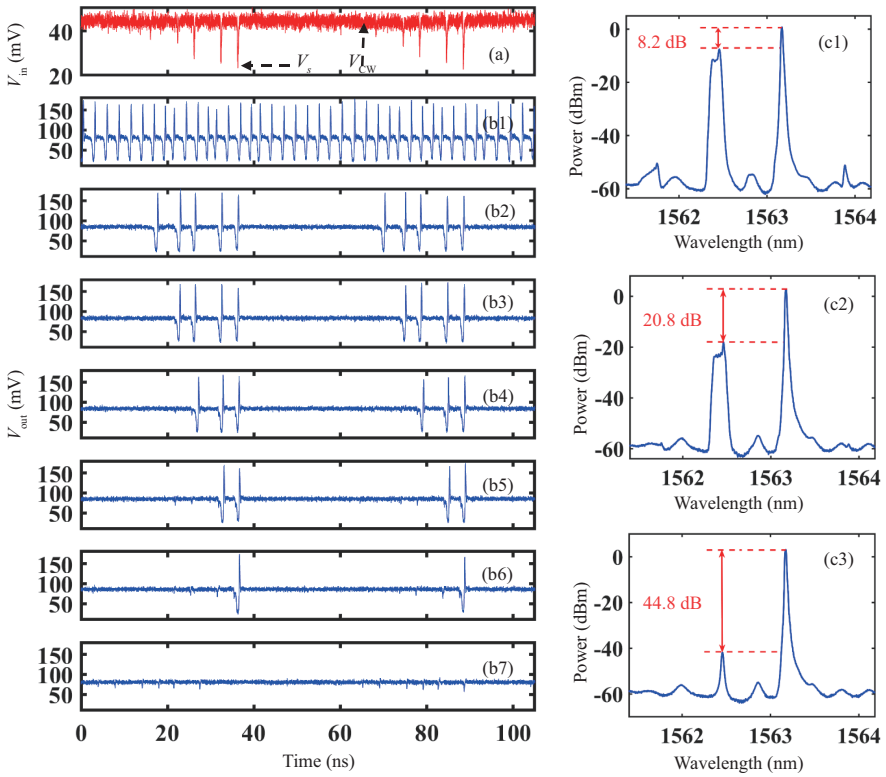

Figure 4 (Color online) Excitability threshold property of the optically-injected DFB. (a) The defined stimulus pulse with different intensities; (b) the corresponding spike response for different injected power. The injected power corresponding to (b1)–(b7) is 360.5, 383.5, 391.9, 411.2, 441.3, 460.4, and 591.8 μW, respectively. (c1)–(c3) corresponds to (b1), (b4), and (b7), respectively, under $I = 61.5$ mA.

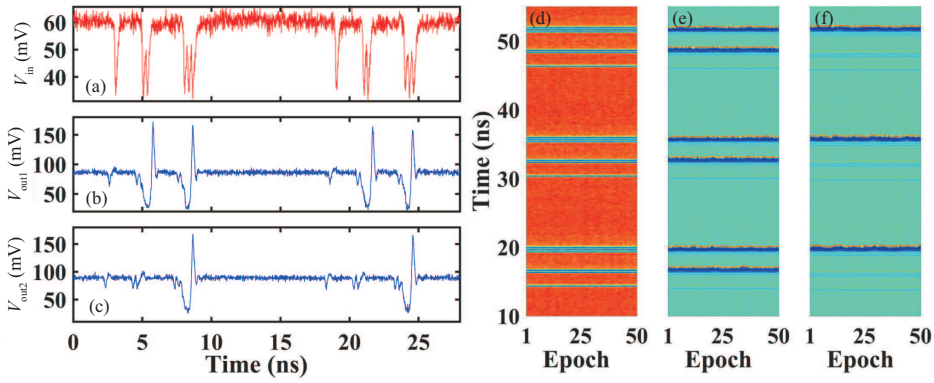

Figure 5 (Color online) Temporal integration behavior of the optically-injected DFB. (a) The defined stimulus pulse burst. The spike response for different injected powers: (b) 452.1 μW and (c) 531.8 μW. (d)–(f) represent temporal maps corresponding to (a)–(c) for 50 consecutive external stimuli.

stimulus pulse cannot trigger a spike response separately. As shown in Figure 5(b), the two closely-spaced pulse burst as well as the three closely-spaced pulse burst can trigger the excitable spike response. This means the stimulus can be integrated temporally. That is, even if the strength for a single stimulus pulse is not sufficiently large, the two closely-spaced pulses can temporally integrate and exceed the excitable spiking threshold. As shown in Figure 5(c), a higher injected power leads to a larger excitable spiking threshold, the spike response can only be generated for the three closely-spaced stimulus pulse bursts. As verified in Figures 5(d)–(f), such a controllable spike response can be reproduced for 50 consecutive arriving external stimuli. Thus, temporal integration can also be realized in the DFB laser subject to SMOPI.

The refractory period is also measured in the following. As shown in Figure 6(a), we define 10 pairs of

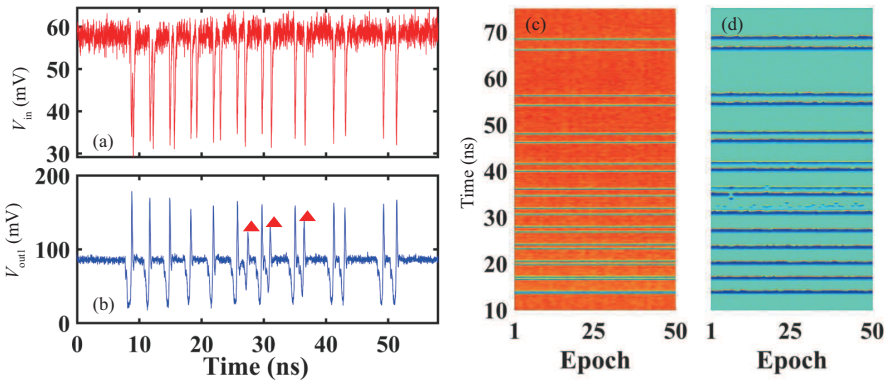

Figure 6 (Color online) Refractory period of the optically-injected DFB. (a) Defined stimulus with 10 pairs of pulses with increasing ISI and (b) the corresponding response; (c) and (d) represent temporal maps corresponding to (a) and (b). The injected power is 452.1 μW.

pulses with gradually-increasing inter-spike-interval (ISI). The time interval is [0.3, 0.5, 0.7, 0.9, 1.1, 1.3, 1.5, 1.7, 1.9, 2.1] ns. Obviously, as can be seen from Figure 6(b), the first 5 pulse pairs each can trigger a single spike response, while the last 5 pulse pairs each can trigger two spikes. Note, for the first 5 pulse pairs, the first stimulus pulse triggers the spike response, as the carrier is consumed and needs time to be recovered, the second stimulus pulse cannot trigger another spike response for ISI $<$ 1.1 ns. Thus, the absolute refractory period is about 1.1 ns, which is about the reciprocal of the self-pulsation frequency that is presented in Figure 3(b). For the last 5 pulse pairs, the time interval is large enough and is greater than the absolute refractory period, thus, both two pulses can separately trigger a spike response. But we can also find that the amplitude of the second spike response is relatively small for the 6-th, 7-th, and 8-th pulse pairs, which can be attributed to the relative refractory period. For the 9-th and 10-th pulse pairs, the response spikes have comparable amplitude. Thus, both the absolute refractory period and the relative refractory period can be realized in the DFB laser-based photonic spiking neuron. The temporal maps shown in Figures 6(c) and (d) indicate that the refractory period property is controllable and repeatable.

In Figure 7, we further demonstrated the simultaneous realization of temporal integration and excitable spike threshold. As presented in Figure 7(a), we define three types of stimulus pulse. The first type is a sub-threshold weak power drop pulse, which cannot trigger a response spike. The second type is a burst of three closely-spaced weak power drop pulses. As can be seen in Figure 7(b), due to the temporal integration effect, a response spike is generated. The third type is a strong power drop pulse that is greater than the excitable spiking threshold, which can trigger a response spike successfully. Besides, we can find that the shapes of the spikes triggered by the second and the third stimulus are the same. The temporal maps presented in Figures 7(c) and (d) further verify the reproducibility of the simultaneous realization of temporal integration and excitable spiking threshold.

Without loss of generality, we also consider the case when the wavelength of optically injected light is near the first side mode. The experimental measurements show that similar excitability and controllable neuron-like spiking response can be achieved. But when the wavelength of the optically injected light matches the peak wavelength of the free-running DFB, the nonlinear dynamics become more complex, and it is difficult to obtain controllable excitable properties. Thus, it is suggested to introduce the SMOPI into the DFB laser to act as a photonic spiking neuron.

4 Numerical model and results

We further verify the experimental findings by using the rate equations model that includes the SMOPI. Here, to consider the effect of the side mode optical injection, we adopt multimode rate equations as follows [47–49]:

$$\frac{\mathrm{d}E_m(t)}{\mathrm{d}t} = \frac{1+\mathrm{i}\alpha}{2}\left[G_m(N) - \frac{1}{\tau_p}\right]E_m(t) + \sqrt{2\beta\xi(t)}$$

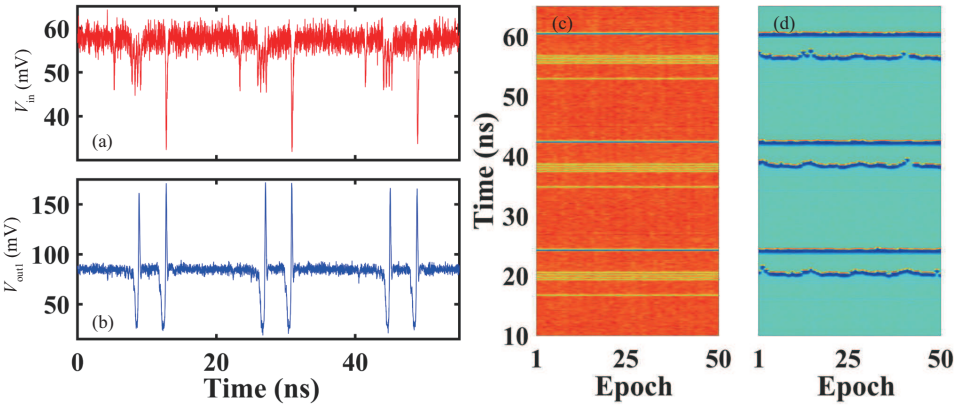

Figure 7 (Color online) Simultaneous demonstration of the temporal integration and spike threshold. (a) Defined stimulus and (b) the corresponding response; (c) and (d) represent temporal maps corresponding to (a) and (b). The injected power is 446.9 μW.

Table 1 Basic parameters used in the simulation [47–49]

Parameters	Symbol	Value
Linewidth enhancement factor	α	3
Differential gain	g_c	3.2×10^3 s^{-1}
Transparency carrier number	N_0	1.25×10^8
Gain saturation coefficient	s	10^{-7}
Total number of modes	M	3
Carrier lifetime	τ_N	1.6 ns
Photon lifetime	τ_p	2 ps
Injection delay	$\tau_{\rm in}$	0
Group index	n_g	3.46
Cavity length	L	1.2 mm
Internal round-trip time	$\tau_L = 1/\Delta f_L$	27.68 ps
Wavelength of mode 0	λ_0	1562.436 nm
Longitudinal mode frequency spacing	$\Delta f_L = c/(2n_g L)$	36.12 GHz
Injection frequency	$f_{\rm in}$	1.197×10^{14} Hz
Frequency detuning	$\delta_f = f_{\rm in} - f_m$	−4 GHz
Gain width	Δf_g	10 THz
Bias current	I	88 mA
Spontaneous emission noise	β	10^{-3}

$$+\frac{k_{\rm in}}{\tau_L}E_{\rm in}(t-\tau_{\rm in})\exp(\mathrm{i}2\pi\delta_f t)\times\exp(-\mathrm{i}2\pi f_{\rm in}\tau_{\rm in}), \tag{1}$$

$$\frac{\mathrm{d}N(t)}{\mathrm{d}t}=\frac{I}{q}-\frac{N(t)}{\tau_N}-\sum_{m=0}^{M-1}G_m|E_m(t)|^2, \tag{2}$$

$$G_m=\frac{g_c(N(t)-N_0)}{1+s\sum_{m=0}^{M-1}|E_m(t)|^2}\left[1-\left(\frac{m\Delta f_L}{\Delta f_g}\right)^2\right], \tag{3}$$

where E, N represent the complex electric field and carrier number, respectively. The subscript m ($M=0,\ldots,M-1$) and "in" denote the m-th mode of the laser and the injected signal, and M is the total number of modes. G_m is the mode gain. I is the bias current. $E_{\rm in}(t-\tau_{\rm in})$ denotes the external optical injection and $k_{\rm in}$ represents the injection coefficient. The other parameters are given in Table 1. Here, the bias current, cavity length, and wavelength of the dominant mode are extracted from our experimental measurements. With these parameters, we numerically solve the rate equations with the fourth-order Runge-Kutta method.

Here, similar to the experimental scheme, the external optical light is injected into the 2-nd mode with a slight negative frequency detuning. Under the CW optical injection, the periodic spike can also be observed (not shown here for simplicity).

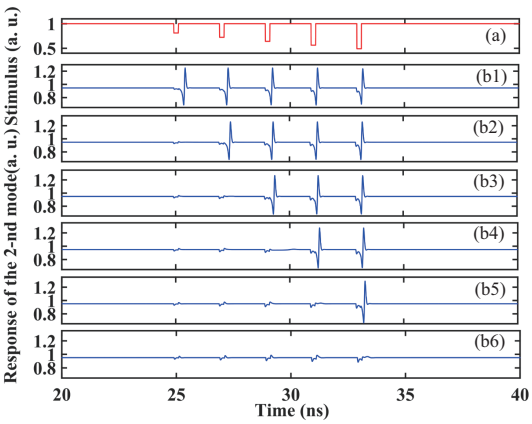

Figure 8 (Color online) Numerical results of controllable response spikes number under SMOPI. (a) The stimuli; (b) the response in the 2nd mode, (b1)–(b6) corresponds to k_{in}=0.215, 0.22, 0.225, 0.23, 0.24, 0.25, respectively.

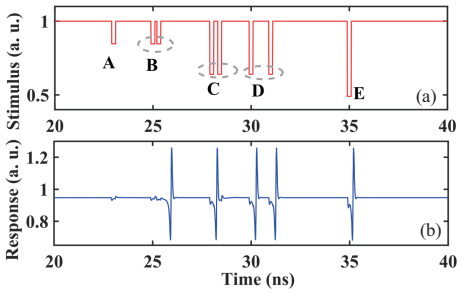

Figure 9 (Color online) Numerical results of temporal integration and refractory period under SMOPI. (a) The stimuli; (b) the response in the 2nd mode, with k_{in}= 0.22.

Then we consider the optical pulse injection which is also encoded into the power drop pulses. As displayed in Figure 8, an obvious spike threshold can be observed. Besides, with the increase of injection coefficient, the spike number is decreased gradually in a controllable way, which agrees well with the experimental findings. Figure 9 further presents the numerical results of simultaneous realization of the temporal integration, refractory, and spike threshold property. It can be seen that the first weak stimulus (denoted as A) does not trigger a spike, while the second stimulus with two closely-spaced weak pulses (denoted as B) can trigger a spike due to the temporal integration effect. The two closely-spaced strong stimulus pulses (denoted as C) only produce a single spike (triggered by the first stimulus pulse) due to the refractory period. While the two stimulus pulses with sufficiently large intervals (denoted by D) can each trigger a response spike. The last strong stimulus pulse triggers a spike with the same amplitude as the other four generated spikes. Thus, the experimental results of neuron-like spiking response can be well produced with our numerical model. With such a numerical model, the hardware-algorithm co-design and optimization can be further performed to improve the performance of the photonic SNN for the practical applications.

5 Conclusion

We proposed and experimentally demonstrated the neuron-like spiking response in a DFB laser subject to SMOPI, based on the transition between the excitability regime and side mode injection-locked state. The controllable and repeatable neuron-like nonlinear computation including excitable spiking threshold, temporal integration, and the refractory period are successfully observed in experiments. The experimental findings are further reproduced with a rate equation model that considers the SMOPI. Thus, the DFB laser with SMOPI can act as a photonic spiking neuron. It is worth mentioning that, the DFB laser fabricated with REC technique is easy to be integrated into large-scale array [42]. Therefore, as a further attempt, the photonic spiking neuron array based on a large-scale DFB laser array deserves further investigation. In addition, with the help of heterogenous or hybrid integration techniques [50], the DFB laser array can act as universal photonics spiking neurons of large-scale photonic SNN chips via integrating with the mainstream synapse weight networks.

Acknowledgements This work was supported by National Key Research and Development Program of China (Grant Nos. 2021YFB2801900, 2021YFB2801901, 2021YFB2801902, 2021YFB2801904, 2018YFE0201200), National Natural Science Foundation of China (Grant No. 61974177), National Outstanding Youth Science Fund Project of National Natural Science Foundation of China (Grant No. 62022062), and Fundamental Research Funds for the Central Universities (Grant No. QTZX23041).

References

1 Roy K, Jaiswal A, Panda P. Towards spike-based machine intelligence with neuromorphic computing. Nature, 2019, 575: 607–617

2 Schuman C D, Potok T E, Patton R M, et al. A survey of neuromorphic computing and neural networks in hardware. 2017. ArXiv:1705.06963

3 Marković D, Mizrahi A, Querlioz D, et al. Physics for neuromorphic computing. Nat Rev Phys, 2020, 2: 499–510
4 Wetzstein G, Ozcan A, Gigan S, et al. Inference in artificial intelligence with deep optics and photonics. Nature, 2020, 588: 39–47
5 Shastri B J, Tait A N, de Lima T F, et al. Photonics for artificial intelligence and neuromorphic computing. Nat Photon, 2021, 15: 102–114
6 Xiang S Y, Han Y N, Song Z W, et al. A review: photonics devices, architectures, and algorithms for optical neural computing. J Semicond, 2021, 42: 023105
7 Guo X H, Xiang J L, Zhang Y J, et al. Integrated neuromorphic photonics: synapses, neurons, and neural networks. Adv Photon Res, 2021, 2: 2000212
8 Huang C, Sorger V J, Miscuglio M, et al. Prospects and applications of photonic neural networks. Adv Phys-X, 2022, 7: 1981155
9 Shen Y, Harris N C, Skirlo S, et al. Deep learning with coherent nanophotonic circuits. Nat Photon, 2017, 11: 441–446
10 Feldmann J, Youngblood N, Karpov M, et al. Parallel convolutional processing using an integrated photonic tensor core. Nature, 2021, 589: 52–58
11 Xu X Y, Tan M X, Corcoran B, et al. 11 TOPS photonic convolutional accelerator for optical neural networks. Nature, 2021, 589: 44–51
12 Xu S F, Wang J, Shu H W, et al. Optical coherent dot-product chip for sophisticated deep learning regression. Light Sci Appl, 2021, 10: 221
13 Zhang H, Gu M, Jiang X D, et al. An optical neural chip for implementing complex-valued neural network. Nat Commun, 2021, 12: 457
14 Tian Y, Zhao Y, Liu S P, et al. Scalable and compact photonic neural chip with low learning-capability-loss. Nanophotonics, 2022, 11: 329–344
15 Zhou H L, Dong J J, Cheng J W, et al. Photonic matrix multiplication lights up photonic accelerator and beyond. Light Sci Appl, 2022, 11: 30
16 Feldmann J, Youngblood N, Wright C D, et al. All-optical spiking neurosynaptic networks with self-learning capabilities. Nature, 2019, 569: 208–214
17 Ashtiani F, Geers A J, Aflatouni F. An on-chip photonic deep neural network for image classification. Nature, 2022, 606: 501–506
18 Hurtado A, Henning I D, Adams M J. Optical neuron using polarisation switching in a 1550nm-VCSEL. Opt Express, 2010, 18: 25170–25176
19 Xiang S Y, Wen A J, Pan W. Emulation of spiking response and spiking frequency property in VCSEL-based photonic neuron. IEEE Photon J, 2016, 8: 1–9
20 Deng T, Robertson J, Hurtado A. Controlled propagation of spiking dynamics in vertical-cavity surface-emitting lasers: towards neuromorphic photonic networks. IEEE J Sel Top Quantum Electron, 2017, 23: 1–8
21 Zhang Y H, Robertson J, Xiang S Y, et al. All-optical neuromorphic binary convolution with a spiking VCSEL neuron for image gradient magnitudes. Photon Res, 2021, 9: B201
22 Robertson J, Hejda M, Bueno J, et al. Ultrafast optical integration and pattern classification for neuromorphic photonics based on spiking VCSEL neurons. Sci Rep, 2020, 10: 6098
23 Robertson J, Zhang Y H, Hejda M, et al. Image edge detection with a photonic spiking VCSEL-neuron. Opt Express, 2020, 28: 37526–37537
24 Xiang S Y, Han Y N, Guo X X, et al. Real-time optical spike-timing dependent plasticity in a single VCSEL with dual-polarized pulsed optical injection. Sci China Inf Sci, 2020, 63: 160405
25 Song Z W, Xiang S Y, Cao X Y, et al. Experimental demonstration of photonic spike-timing-dependent plasticity based on a VCSOA. Sci China Inf Sci, 2022, 65: 182401
26 Nahmias M A, Shastri B J, Tait A N, et al. A leaky integrate-and-fire laser neuron for ultrafast cognitive computing. IEEE J Sel Top Quantum Electron, 2013, 19: 1–12
27 Xiang S Y, Zhang Y H, Gong J K, et al. STDP-based unsupervised spike pattern learning in a photonic spiking neural network with VCSELs and VCSOAs. IEEE J Sel Top Quantum Electron, 2019, 25: 1–9
28 Xiang S Y, Ren Z X, Song Z W, et al. Computing primitive of fully VCSEL-based all-optical spiking neural network for supervised learning and pattern classification. IEEE Trans Neural Netw Learn Syst, 2020, 32: 2494–2505
29 Selmi F, Braive R, Beaudoin G, et al. Relative refractory period in an excitable semiconductor laser. Phys Rev Lett, 2014, 112: 183902
30 Pammi V A, Alfaro-Bittner K, Clerc M G, et al. Photonic computing with single and coupled spiking micropillar lasers. IEEE J Sel Top Quantum Electron, 2020, 26: 1–7
31 Peng H T, Nahmias M A, de Lima T F, et al. Neuromorphic photonic integrated circuits. IEEE J Sel Top Quantum Electron, 2018, 24: 1–15
32 Peng H T, Angelatos G, de Lima T F, et al. Temporal information processing with an integrated laser neuron. IEEE J Sel Top Quantum Electron, 2020, 26: 1–9
33 Xiang S Y, Shi Y C, Guo X X, et al. Hardware-algorithm collaborative computing with photonic spiking neuron chip based on an integrated Fabry-Perot laser with a saturable absorber. Optica, 2023, 10: 162
34 Song Z W, Xiang S Y, Guo X X, et al. Nonlinear neural computation in an integrated FP-SA spiking neuron subject to incoherent dual-wavelength optical pulse injections. Sci China Inf Sci, 2023, 66: 229405
35 Xiang J L, Zhang Y J, Zhao Y T, et al. All-optical silicon microring spiking neuron. Photon Res, 2022, 10: 939
36 Xiang J L, Torchy A, Guo X H, et al. All-optical spiking neuron based on passive microresonator. J Lightwave Technol, 2020, 38: 4019–4029

37 Jha A, Huang C, Peng H T, et al. Photonic spiking neural networks and graphene-on-silicon spiking neurons. J Lightwave Technol, 2022, 40: 2901–2914

38 Chakraborty I, Saha G, Roy K. Photonic in-memory computing primitive for spiking neural networks using phase-change materials. Phys Rev Appl, 2019, 11: 014063

39 Prucnal P R, Shastri B J, Ferreira de Lima T, et al. Recent progress in semiconductor excitable lasers for photonic spike processing. Adv Opt Photon, 2016, 8: 228

40 Zhao A K, Jiang N, Peng J F, et al. Parallel generation of low-correlation wideband complex chaotic signals using CW laser and external-cavity laser with self-phase-modulated injection. Opto-Electron Adv, 2022, 5: 200026

41 Ma B W, Zou W W. Demonstration of a distributed feedback laser diode working as a graded-potential-signaling photonic neuron and its application to neuromorphic information processing. Sci China Inf Sci, 2020, 63: 160408

42 Shi Y C, Li S M, Chen X F, et al. High channel count and high precision channel spacing multi-wavelength laser array for future PICs. Sci Rep, 2014, 4: 7377

43 Shi Y C, Ma Y X, Hong Z M, et al. High-power DFB semiconductor laser array. In: Proceedings of International Conference on Optical Instruments and Technology: Optical Communication and Optical Signal Processing, 2021

44 Wieczorek S, Lenstra D. Spontaneously excited pulses in an optically driven semiconductor laser. Phys Rev E, 2004, 69: 016218

45 Wieczorek S, Krauskopf B, Lenstra D. Multipulse excitability in a semiconductor laser with optical injection. Phys Rev Lett, 2002, 88: 063901

46 Wieczorek S, Krauskopf B, Simpson T B, et al. The dynamical complexity of optically injected semiconductor lasers. Phys Rep, 2005, 416: 1–128

47 Yang Q, Wu Z M, Wu J G, et al. Influence of injection patterns on chaos synchronization performance between a multimode laser diode and a single-mode laser. Opt Commun, 2008, 281: 5025–5030

48 Ryan A T, Agrawal G P, Gray G R, et al. Optical-feedback-induced chaos and its control in multimode semiconductor lasers. IEEE J Quantum Electron, 1994, 30: 668–679

49 Zhang Y T, Jia Z W, Li Q T, et al. Broadband chaos signal generation based on dual-mode DFB laser with optical feedback (in Chinese). Acta Opt Sin, 2021, 41: 2114001

50 Hao Y, Xiang S Y, Han G Q, et al. Recent progress of integrated circuits and optoelectronic chips. Sci China Inf Sci, 2021, 64: 201401